JOURNAL OF SPACECRAFT AND ROCKETS
Vol. 45, No. 6, November–December 2008

Ground Test Studies of the HIFiRE-1 Transition Experiment Part 1: Experimental Results

T. P. Wadhams,* E. Mundy,† M. G. MacLean,‡ and M. S. Holden§
Calspan—University at Buffalo Research Center, Buffalo, New York 14225

DOI: 10.2514/1.38338

As part of a two-phase experimental study to obtain detailed heating and pressure data over the full-scale hypersonic international flight research and experimentation (HIFiRE-1, formally FRESH FX-1) flight geometry, Calspan—University at Buffalo Research Center has completed a matrix of ground tests to determine the optimal flight geometry and instrumentation configuration necessary to make measurements of desired flow phenomena during the flight experiment. The primary objective of the HIFiRE-1 flight experiment is to collect high-quality flight data from integrated flight instrumentation to be used for computational fluid dynamic code and ground test facility validation in regions of boundary-layer transition, turbulent separated flow, and shock/boundary-layer interaction. To support this flight experiment, data have been obtained in the large energy national shock hypervelocity wind tunnel employing a full-scale model over a range of Mach numbers from 6.5 to 7.4 and Reynolds numbers from 0.5E + 06 to 5.5E + 6 duplicating the reentry trajectory. These points gave researchers the best chance to measure the transition process on the forecone and have a turbulent separated flow on the cylinder that reattached onto the flare section. These test condition ranges were determined directly from the nominal descent trajectory of the Australian-launched Terrier–Orion launch vehicle that will serve as the booster for HIFiRE-1. The entire experimental database will be compared to future flight data and used by computationalists to validate codes in regions of attached and separated laminar and turbulent flows with shock/boundary layer interaction. In addition to the experimental data, Calspan—University at Buffalo Research Center performed a large amount of computational fluid dynamic analyses to confirm and validate not only the tunnel flow conditions, but also the two- and three-dimensional flows over the model itself. These detailed computational results will be presented in a Part 2 companion paper.

I. Introduction

EXPERIMENTAL and computational studies have been conducted in two distinct phases by the Calspan—University at Buffalo Research Center (CUBRC) Aerothermal Aero-Optic Evaluation Center (AAEC) team to assist in the selection of a blunted cone/cylinder/flare configuration to be employed in the U.S. Air Force Office of Scientific Research (AFOSR)/U.S. Air Force Research Laboratory (AFRL) sponsored hypersonic international flight research and experimentation (HIFiRE-1) flight-test program. The objective of the first phase of the ground test program was to select nose-tip and flare geometries that give researchers the best chance to obtain boundary-layer transition, turbulent separated flow, and shock wave/boundary-layer interaction data in flight. The ground test and flight results will represent an important database to evaluate the prediction methods that describe these classes of hypersonic flows. CUBRC's large energy national shock (LENS I) hypervelocity tunnel was selected to meet these objectives because of the facility's capability of duplicating the required freestream conditions while testing a full-scale version of the flight vehicle. Freestream conditions for these studies were selected from the trajectory of the Australian Terrier–Orion booster, the launch vehicle for the flight test, at points where transition would occur in a desirable location on the cone. The angle of attack measurements were also obtained as they pertain to the expected trajectory to explore the three-dimensional transition and shock/wave turbulent boundary-layer interaction effects the vehicle will experience in flight. Additionally, high-speed schlieren movies were taken of the flare region to assess the separated region length for variations in flare angle, freestream condition, and model attitude. The flare was not instrumented in this first phase of the program to allow the geometry, specifically the angle, to be changed with minimal downtime between tests. The first-phase experiments resulted in a blunt 2.5 mm nose and flare angle of 33 deg, which will be the eventual flight geometry.

The second phase of the ground test program, which is described in detail in this paper, was designed to obtain additional higher-resolution data in the transition region, to obtain pressure and heat-flux data in the flow separation/interaction region over the flare, and to study the effects of a discreet diamond roughness element on the transition process. The heat-flux results and high-speed schlieren video from the first phase were directly employed to place the additional instruments. These additional heat-flux instruments more than doubled the number of heat-flux sensors and represented sufficient resolution for code validation efforts. The first several experiments were performed using duplicate conditions and model geometry from the first phase to verify that the new results compared favorably to those already obtained. These tests showed that, although the data on the cone and cylinder sections agreed with the results from the first entry, the flare results showed that, for the flight flare length, the data lacked an appreciable plateau region behind the interaction peak to be used as a boundary condition for computationalists. An extended-length flare was constructed, and the test program proceeded normally, obtaining a data set capable of validating the computational methods and comparing it to the flight results. The second phase of the ground test also included the addition of a diamond roughness element to the cone surface. This trip was designed to extend the duration of the flight test so that turbulent results could be obtained. The flight-test plan calls for the

Presented as Paper 0639 at the 46th Aerospace Sciences Meeting & Exhibit., Reno, NV, 7–10 January 2008; received 30 April 2008; revision received 28 August 2008; accepted for publication 29 August 2008.

*Research Scientist, Aerothermal/Aero-Optic Evaluation Center, 4455 Genesee Street. AIAA Member.
†Research Engineer, Aerothermal/Aero-Optic Evaluation Center, 4455 Genesee Street. AIAA Member.
‡Senior Research Scientist, Aerothermal/Aero-Optic Evaluation Center, 4455 Genesee Street. AIAA Member.
§Program Manager, Aerothermal/Aero-Optic Evaluation Center, 4455 Genesee Street. AIAA Fellow.

trip to be placed on only one side of the flight vehicle and, hence, only produce turbulent flow on that side with a laminar or smooth body transition on the other side. This flight state required ground testing to verify that the effects of the trip did not feed to the other side of the model over a range of Reynolds numbers and model attitudes. The secondary objectives of the experimental study included obtaining detailed high-speed schlieren movies of the boundary-layer transition on the cone, employing time-of-arrival pressure transducers to obtain second-mode transition frequencies, and making pitot pressure measurements to characterize the level and frequency of the fluctuating pressure component due to the turbulent boundary layer on the facility nozzle wall.

In a similar fashion to what was done in the first phase, CUBRC also performed a large amount of computational work to assess both the flow in the test facility and the freestream flow over the model. These computational results include laminar and turbulent predictions of the pressure and heat transfer on the cone and cylinder sections employing the DPLR code and stability calculations of the forebody using stability and transition analysis for hypersonic boundary layers (STABL). New to this phase is an assessment of turbulence models and the prediction of turbulent flow in regions of separation, reattachment, and shock/boundary-layer interaction. This work will be briefly mentioned here but has been described in detail in [1]. Finally, new e^N-method STABL calculations will be made with the additional heat-flux instrumentation results to assess if this higher-resolution data set has an influence on the interpretation of laminar–turbulent transition onset.

II. Facilities and Instrumentation

A. The LENS Facility

The aerothermal tests in this program were performed in the LENS I hypervelocity reflected shock tunnel (HST). A schematic diagram of the LENS I HST is shown alongside the LENS II and X facilities in Fig. 1. The three facilities share a common control system, compressor system, data recording system, and data analysis system. LENS I was constructed with the capability of fully duplicating flight conditions at Mach numbers ranging from 6 to 15 to conduct testing with full-scale versions of missile interceptors and scramjet engines. The major components of the LENS I facility include a 25.5 ft long by 11-in.-diam electrically heated driver tube, a double diaphragm assembly, a 60 ft by 8-in.-diam driven tube, a fast-acting center-body valve assembly, multiple nozzles to achieve desired test conditions from Mach 6 to 18, and a test section capable of accommodating models up to 3 ft in diameter and 12 ft long. A new nozzle upgrade will soon take this capability up to Mach 22. The high-pressure driver section of LENS I has the capacity to operate at $30,000\ \mathrm{lbf/in.}^2$ using heated driver gases of hydrogen, helium, nitrogen, or any combination of the three. The driver gases can be heated up to 750°F and the amount of each gas varied to achieve tailored interface operations for maximum test times. The driven tubes of either facility can use air, nitrogen, carbon dioxide, helium, hydrogen, or any other gases or combinations of gases for model testing.

A schematic diagram illustrating the basic operation of the shock tunnel is shown in Fig. 2. Both LENS I and II tunnels operate with tailored interface conditions to maximize test condition uniformity and run time. Tailored conditions are achieved by carefully controlling the pressures and gas mixtures used in the driver and driven tubes of the tunnel to achieve a condition under which the contact surface between the driver and driven gases is transparent to the reflected shock. Flow is initiated through the tunnel by rapidly pressurizing the center section of the double diaphragm unit, causing the diaphragms to rupture. The sudden release of the driver gas generates a strong shock that travels down the driven tube, is reflected from the end wall, and travels back up the driven tube, creating a stagnant, high-pressure, high-temperature reservoir of test gas. When the reflected shock strikes the interface in its return path, the condition in the driver and driven tubes are controlled such that the contact surface is brought to rest. The reservoir of hot stationary test gas between the end wall and the contact surface is exhausted through the throat section of the nozzle into the test section in a manner similar to any blowdown tunnel. The flow through the nozzle is terminated when a fast-acting valve closes the throat section.

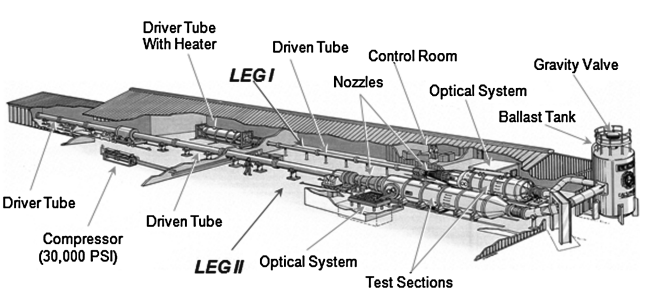

Fig. 1 Schematic drawing of the LENS I and II hypersonic shock tunnel facilities and the LENS X expansion.

A velocity/altitude map for the LENS facilities is shown in Fig. 3. This map includes the ascent and descent trajectories of the Australian Terrier–Orion launch vehicle that will serve as the booster for HIFiRE-1. The stars represent the test points of interest in this study duplicating the freestream conditions the vehicle will experience in flight. By operating the LENS tunnel under cold conditions (just above the liquefaction temperature of the airflow in the test section), large Reynolds numbers and test times can be obtained in the LENS I facility for studies in which only the Mach and Reynolds number simulation is required. A Reynolds and Mach number performance plot for the LENS facility, again including the HIFiRE-1 trajectory, is shown in Fig. 4. A complete listing of LENS facility capabilities can be found in [2].

B. Heat Transfer Instrumentation

For these studies, we primarily employed platinum thin-film heat transfer instrumentation similar to that designed at the Cornell Aeronautical Laboratory in the late 1950s and refined over the past 50 years [3,4]. The platinum thin-film heat transfer instrumentation employed in these studies has proven to be the most accurate measurement technique in supersonic and hypersonic test facilities, and the small size of the sensing element coupled with the insulating substrate make it ideal for measuring high-resolution heating levels and the spacing of the heating on the surface of the model. CUBRC has calculated the accuracy of the heat transfer measurement to be $\pm 5\%$.

The thin-film heat transfer gauge is a resistance thermometer that measures the local surface temperature of the model. The theory of heat conduction is used to relate the surface temperature history to the rate of heat transfer. Because the platinum resistance element has a negligible heat capacity and, hence, a negligible effect on the Pyrex® surface temperature, the gauge can be characterized as being homogeneous and isotropic with properties corresponding to those of the Pyrex®. Furthermore, because of the short duration of shock tunnel tests, the Pyrex® can be treated as a semi-infinite body. Examples of the types of thin-film instrumentation employed in this test can be seen in Figs. 5 and 6. Because of the requirement to obtain transitional data in this program, all the thin-film sensors needed to be specially matched and contoured to the surface of the model. Using very small sensors (Fig. 5b) on the cone section (Fig. 6) greatly helped to achieve an acceptably smooth model. There is the potential to obtain erroneous transition data from any misaligned sensors tripping or disturbing the flow.

The platinum thin-film sensor, with a frequency response of over 500 kHz, is also ideal in obtaining fluctuating heat transfer levels. This information is important to defining the transitional flow characteristics of the model. If an adequate amount of sensors are placed in the transition zone, the transition process can be accurately followed from the initial disturbances, to the turbulent bursts, to the fully turbulent levels. Typically, transition is viewed as occurring at a particular geometric point, but in real life the transition front can be described as moving forward and backward over time or as a series of

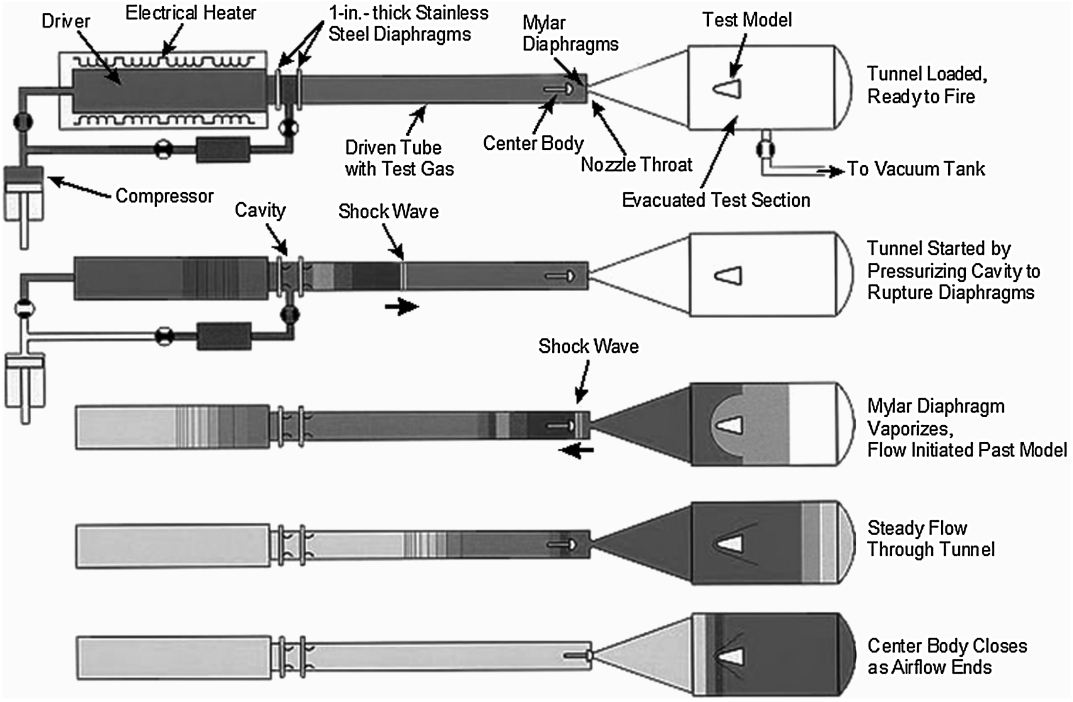

Fig. 2 Basic operation of LENS.

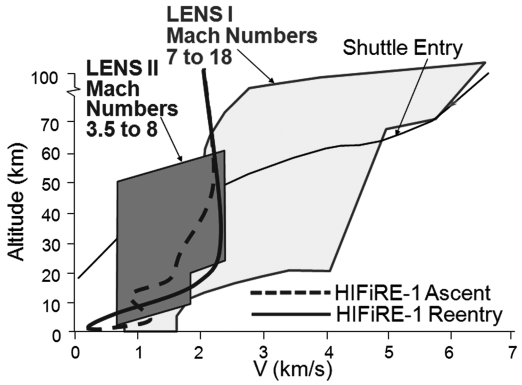

Fig. 3 LENS facility altitude velocity map.

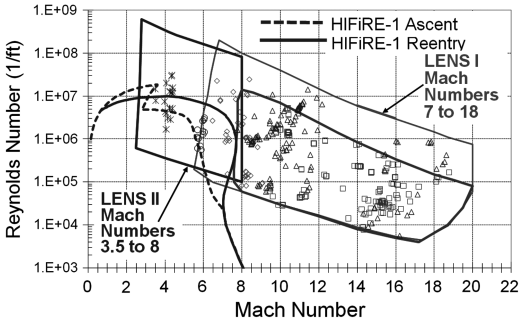

Fig. 4 Mach/Reynolds number envelope.

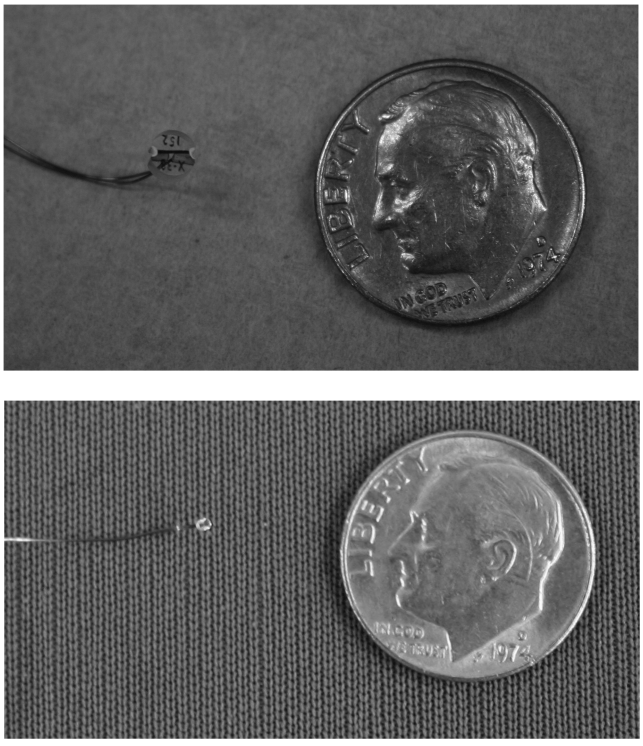

Fig. 5 Thin-film heat transfer instrument: a) 0.125 in., and b) 0.040 in.

bursts that break out and move downstream. The thin-film sensor is the most accurate method of describing the limits of the movement and the associated heating rates.

During the first phase of the experimental program, the model contained over 50 platinum thin-film sensors, distributed along the length of the model and at 0, 90, 180, and 270 deg around the model. This number was doubled between entries to over 100 sensors, of which 30 were placed in the cone/flare region to accurately measure the separation/reattachment flow.

C. Pressure Instrumentation

For these studies, we primarily employed piezoelectric pressure gauge instrumentation that, like the platinum thin-film sensor, was originally designed at the Cornell Aeronautical Laboratory. These gauges employ a diaphragm design and read the model pressure vs a pretest baseline pressure (differential pressure). In the data reduction process, this baseline, or prerun pressure, is subtracted from the final measurement to yield an absolute measurement. Additionally, these transducers are mounted close to the surface of the test article so that orifice effects and fill times are negligible. The piezoelectric pressure transducers, manufactured by PCB®, are capable of accurately

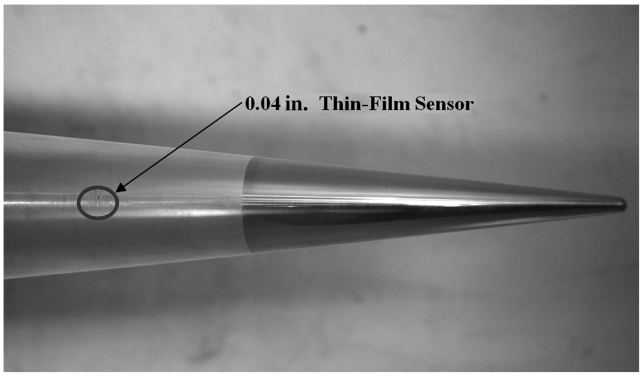

Fig. 6 The 0.04 in. thin-film sensors placed in the HIFiRE-1 nose cone.

measuring pressures within ±3%. Figure 7 shows a typical PCB® piezoelectric pressure transducer.

Where size constraints do not allow for PCB®-style instrumentation, CUBRC employs both Endevco and Kulite piezoresistive-type transducers. These transducers have a very small sensing footprint and can be installed in difficult geometry locations. These sensors also typically have a higher frequency response (∼100 kHz) than the standard piezoelectric sensors we employ. The piezoresistive strain gauge-type transducer also has an accuracy of ±3%. Figure 8 shows a typical Kulite-style transducer.

Pressure gauges employed by CUBRC are calibrated after they are installed in the test article whenever possible. Calibration is carried out by subjecting each gauge to a traceable, steady pressure pulse lasting tens of milliseconds to duplicate what the gauge will experience during testing. This will occur over the range of expected pressures that the gauges will experience during testing.

Unique to this test is the use of a PCB® time of arrival pressure sensor for the measurement of second mode transition frequencies. These sensors are of the type PCB® 132A32 and are coupled with PCB® 482A22-type signal conditioners. This combination has been reported in other studies to have successfully measured second mode frequencies, but the goal of this program is to attempt to measure these frequencies at flight-duplicated altitude and velocity conditions [5].

Fig. 7 Typical PCB® piezoelectric pressure transducer.

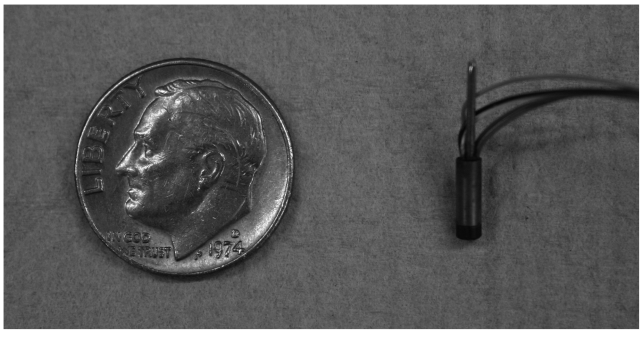

Fig. 8 Typical Kulite piezoresistive transducer.

III. Model Design and Construction

The basic geometry for the HIFiRE-1 flight vehicle was given to CUBRC by the AFRL and is shown in Fig. 9 [6]. The geometry consists of a blunt nose, 7 deg cone, flat cylinder section, a short 33 deg flare section, and another flat cylinder aft end that ties into the booster. The CUBRC model represents a full-scale match of this configuration minus the slot that can be seen in the flare section. This slot will be present in the flight geometry to perform inlet mass capture optical measurements as they might relate to scramjet design. At this time it was deemed unnecessary to include this portion of the program in the CUBRC ground test. All model hardware components were machined on site at CUBRC and the as-built model is shown in Fig. 10. This original configuration had a removable sharp nose and a 37 deg flare section, both of which could be easily changed while the model was in the tunnel. Additional blunt noses of radius 0.098 (2.5) and 0.197 in. (5.0 mm) were also manufactured. All the noses had considerations made for the inclusion of an electrical resistance cartridge heater that would be used to heat the nose to predicted flight temperatures so that wall temperature effects could be studied. The temperature was monitored with several thermocouples embedded in the nose material and,

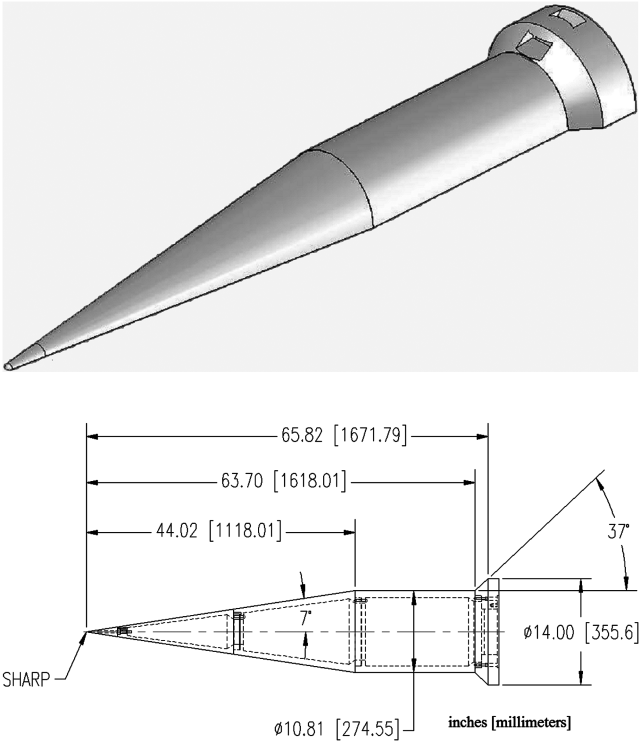

Fig. 9 Basic HIFiRE-1 flight geometry.

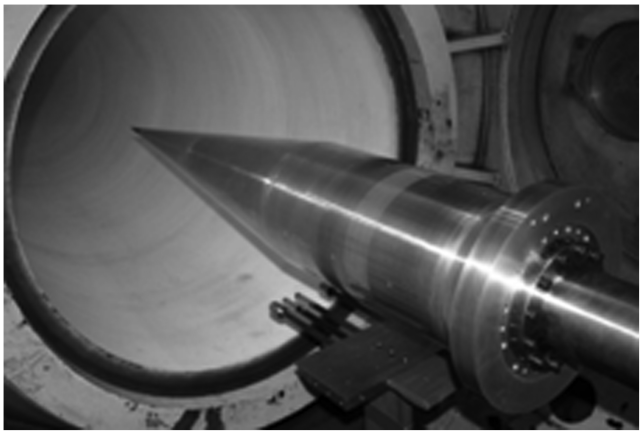

Fig. 10 The as-built HIFiRE-1 installed in LENS I.

additionally, the thin-film instrumentation installed in the cone was employed to specify the temperature profile down the length of the cone. CUBRC also constructed additional flare angles of 27, 30, and 33 deg. Although the 37 deg flare angle was supported by the preliminary numerical predictions, our correlations based on our earlier studies of shock wave/turbulent boundary-layer interaction [7–9] suggested that this angle was too large and that flare angles between 30 and 33 deg would achieve the required well-defined turbulent interaction region at the cylinder/flare junction. To assess the flare angle effectiveness during the first phase of the program, we employed high-speed schlieren video coupled with the results from earlier related studies to suggest the flare angle that should be employed on the flight vehicle. An installation diagram and photograph of the model installed in the LENS I facility is shown in Fig. 11. After the conclusion of the first phase, data analysis concluded that the optimal flight configuration should consist of the 0.098 in. (2.5 mm) nose tip and the 33 deg flare to achieve the goals of the flight test. This configuration would be employed almost exclusively in the second phase of the ground test. The first-phase results were also used to identify the placement of additional heat-flux sensors, including in the transition region on the cone and on a large amount of instrumentation in the cylinder/flare junction region to accurately measure the heat flux due to separation and shock interaction. A photograph of the cylinder/flare region can be seen in Fig. 12.

IV. Selection of Freestream Conditions and Facility Flow Calibrations

The HIFiRE-1 flight trajectory as specified to CUBRC by AFRL is shown in Figs. 13 and 14 and taken from a conference paper by Kimmel et al. [6]. Data will be taken over the entire flight from launch until such a time as the vehicle or sensors fail during descent. The points at which ideal transition conditions exist, at Mach numbers of 6.5 and 7.2, are marked with open stars; they are also listed in Table 1 and compared with the actual conditions employed during the experiment. Other test points matching the flight Mach 7.2 condition but with lower Reynolds numbers of 2, 1, and 0.5 million per foot were added during the second entry to assess trip effectiveness. How these points fall into LENS capabilities is shown in Figs. 3 and 4. All experiments, excluding one test from the first phase, were performed with a room-temperature model wall near 530°R. Each of the unique freestream test conditions that are to be run during the experimental program are first predicted computationally and then calibrated with test runs in the facility. The computational tool employed for these facility nozzle solutions is a specialized version of the DPLR code that has been specifically hardwired for the LENS facility. Further information concerning the DPLR code can be found in Sec. VII.A of this paper. Ultimately the computational work allows for having to make fewer calibration runs at each condition and, more importantly, it adds greatly to the understanding of what is happening in the freestream at every condition. This will be important later when full-model computations are performed.

The experimental calibrations of the LENS facility employ a basic suite of instrumentation including pressure sensors to monitor the initial driver and driven gas pressures and temperatures, thin-film resistance and piezoelectric pressure sensors installed at fixed locations on the driven tube to monitor the speed of the incident shock wave as it propagates down the driven tube, pressure sensors in the end wall region to measure the reflected shock reservoir pressure, a pressure sensor in the initially evacuated test section, and a survey rake installed in the test section to measure pitot pressure, static pressure, and stagnation-point heat transfer in the freestream. From these measurements and the rake assembly, a comprehensive data set for each test condition was obtained to assess freestream conditions and the core flow size and uniformity. A typical survey rake assembly is shown in Fig. 15 together with the flowfield survey probes at the exit plane of the nozzle. The rake may be translated upstream into the

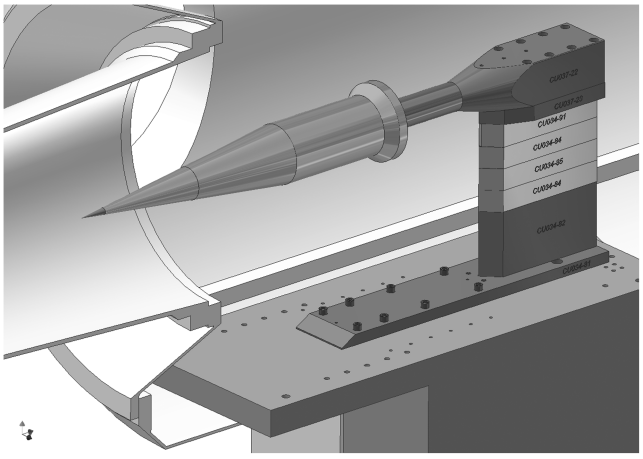

Fig. 11 Drawing of installed HIFiRE-1 model in LENS I.

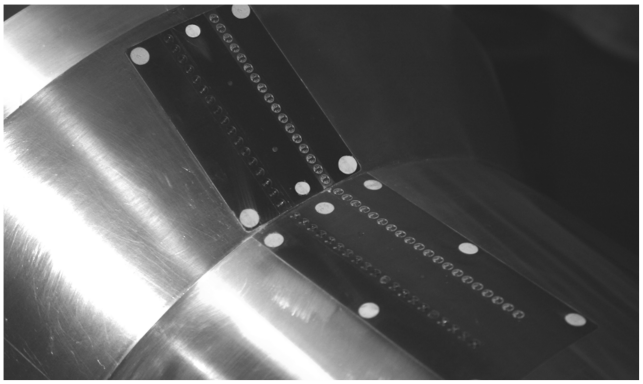

Fig. 12 Second-phase high-fidelity flare instrumentation.

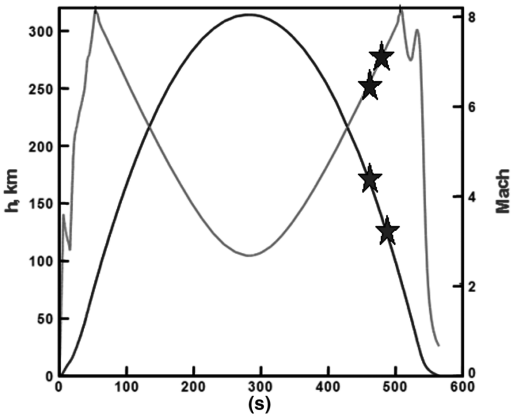

Fig. 13 Overall flight trajectory of HIFiRE-1.

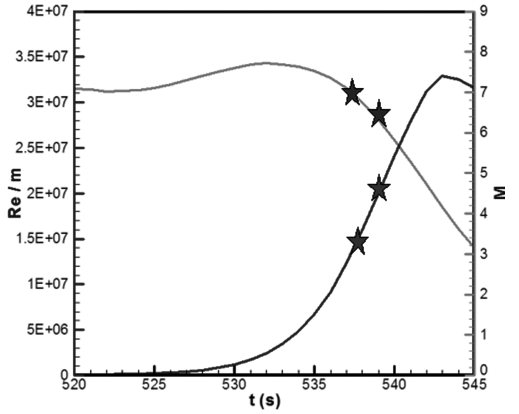

Fig. 14 Detailed Mach/Reynolds number trajectory plot showing area of interest for transition experiments.

Table 1 HIFiRE-1 flight conditions compared with experimental freestream conditions

	Condition A		Condition B	
Freestream condition	Flight	Experiment	Flight	Experiment
Mach number	6.58	6.59	7.16	7.09
Velocity, ft/s	6320	6296	7160	7115
Temperature, °R	386	379	417	417
Pressure, psia	1.12	1.11	0.67	0.68
Density, slugs/ft^3	2.40E − 04	2.45E − 04	1.40E − 04	1.36E − 04
Reynolds number, 1/ft	5.30E + 06	5.31E + 06	3.10E + 06	3.08E + 06

nozzle or downstream into the test section to survey the entire region the test article will occupy.

The freestream conditions in the LENS facility are determined first by specifying the conditions observed in the reservoir. This is accomplished via a combination of measurement and theory. The initial and final (reservoir) pressures are measured by a group of redundant pressure gauges in the end wall of the driven tube. The shock speed is also measured by a series of fast-response gauges down the length of the driven tube that react as the incident shock moves through the test gas. Using these pieces of information, the unique reservoir conditions may be computed from generalized equilibrium conditions and wave propagation theory after both the incident and the reflected shocks have passed through the test gas. The computation of the reservoir assumes full thermodynamic and chemical equilibrium at all points. This is a safe assumption, as the pressures and temperatures after the shocks are very large, thus making relaxation times exceptionally short. Relevant translational, rotational, and vibrational modes are considered in the energy of the molecules. The determined total reservoir conditions are passed through a converging/diverging nozzle and expanded to the measured pitot pressure conditions. This allows the calculation of the Mach number. Freestream velocity, temperature, pressure, density, viscosity, and Reynolds number are then computed from the Mach number and total conditions in the reservoir. Nonequilibrium chemistry effects for the conditions are also calculated employing a heritage Cornell Aeronautical Lab 1-D nozzle code and checked with the DPLR nozzle code Navier–Stokes calculations. For the conditions considered in this paper, the effects of nonequilibrium chemistry have been observed to be negligible. The freestream Mach number uncertainty has been calculated to be less than 0.5%, with temperature and pressure at 3 and 1%, respectively.

The experimental results are then compared with the precalibration computational results. Figure 16 shows a typical example of the comparison between the DPLR Navier–Stokes nozzle solution and the measured pitot profile measurements for the Mach 6.5 flight condition. Pitot pressure in general is used as a measure of freestream accuracy for two primary reasons: 1) it is a directly measurable quantity, and 2) it is sensitive to the momentum in the flowfield. Hence, it is a good choice to judge the accuracy of the freestream specification. This particular profile was taken in the test section of the LENS I facility at a position near the center of the HIFiRE-1 test article. This is an excellent example of the typical level of agreement obtained between computational fluid dynamics (CFD) and the experiment in the LENS facility. The stagnation heat transfer measurements made during the calibrations are also compared with both Fey and Riddell values and the Navier–Stokes solution as an independent verification of the calculated total temperature. In some cases the total temperature of the reservoir is measured directly, but this was not the case in this program due to the total temperature being sufficiently higher than the capability of the probes currently employed at CUBRC.

Pitot pressure measurements were also made to assess the fluctuating pressure component as a percentage of the total pressure that exists in the freestream flow. This fluctuation pressure component originates from the turbulent boundary layer that exists on the wall of the facility nozzle during the test. To obtain this information, two different pitot pressure probes were designed. The first was a flush face probe that allowed the pressure transducer sensing surface to be fully exposed to the flow and able to measure both the pitot pressure and the fluctuating component. The second

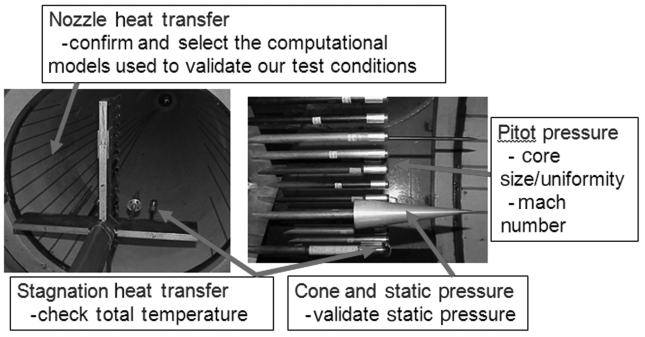

Fig. 15 Calibration rake mounted inside the test section of the LENS I.

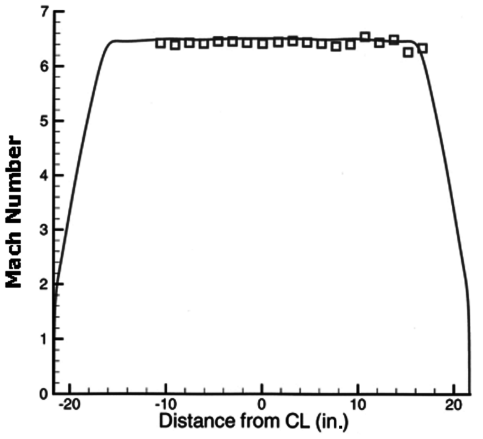

Fig. 16 Comparison between the experimental and computational nozzle profiles.

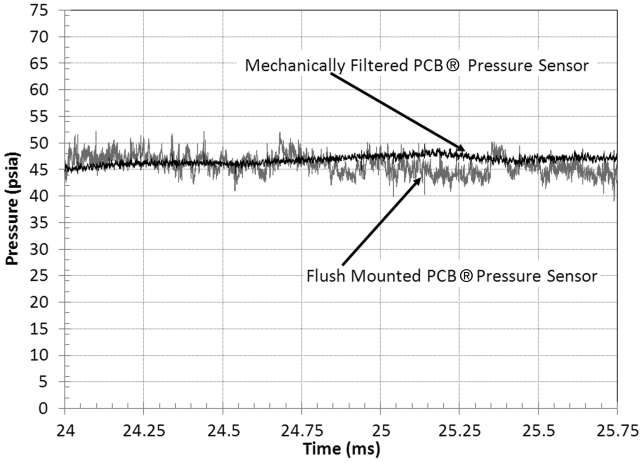

Fig. 17 Time history traces of "filtered" and flush-mounted pitot pressure sensors.

probe was designed to "filter" the fluctuating pressure component out of the measurement by placing the sensing surface of the pressure transducer at the bottom of a cavity inside the probe, which is fed by only a small hole in the front face of the probe. The same pressure transducer type, PCB® 101A06, was employed in both cases and is capable of measuring frequencies of up to 400 kHz. Figure 17 shows the results of the flush-mounted and filtered measurements made during calibration of the Mach 7.2 flight condition. The rms values of both signals were obtained, and from the difference it can be determined that the fluctuating pressure level for these freestream conditions is between 0.25 and 0.5% of the pitot pressure. Figure 18 shows the frequency content of the flush measurement and is especially encouraging in that the frequencies present in the fluctuating pressure component are much less (30–40 kHz) than the predicted second mode frequency (650 kHz) and should be decoupled from influencing the transition process on the model. The second mode frequencies were determined by employing the STABL code that is summarized in Sec. VII.B.

V. Review of Experimental Results from Phase I

The first part of the ground test program [10] concentrated on specifying the nose-tip bluntness that provides well-defined laminar, transitional, and turbulent regions on the cone section for the two flight freestream conditions at Mach 6.5 and 7.2, including several angle of attack variations. The initial tests at both conditions employing a sharp nose tip produced transition locations forward of the nose-tip junction, too far forward to be a definable condition for flight. The next configuration employed a 0.197 in. (5 mm) blunt nose radius that pushed the transition point back near the cone/cylinder junction point. The now-shortened turbulent portion of the cone flow was determined to be too short to be a definable situation in flight. Finally, a bluntness of 0.098 in. (2.5 mm) was tested, giving the results presented in Figs. 19 and 20 for both the Mach 6.5 and 7.2 flight conditions. Here, both definable laminar and turbulent regions are present. To confirm this assertion of laminar and turbulent flow, the semi-empirical prediction methods of Van Driest [11] (turbulent) and Cheng et al. [12] (laminar) are employed on the cone section of the model. Despite the model being blunt, good agreement is shown for both regions, confirming the laminar and turbulent levels. Detailed DPLR Navier–Stokes solutions by MacLean et al. [1] were also completed and show excellent agreement for the laminar portion of the flow. Pressure results were checked with simple Newtonian calculations and again show good agreement with the experimental results and confirm the specified freestream conditions.

Also in this phase of experiments, heat transfer and pressure measurements were obtained for angles of attack of 1 and 5 deg at the Mach 7.2 flight freestream conditions. The flight program is designed to stay within angles of attack of 1 and 2 deg, but for the ground test the extreme angle of 5 deg was selected. These experiments were performed exclusively with the 0.098-in.-radius nose to further validate the decision to employ this bluntness in flight. The heat transfer measurements for the two attitudes tested on the windward side of the model demonstrate that transition moves forward with an increasing angle of attack until, at a model attitude of 5 deg, transition begins close to the nose tip and it is completed at the 15 in. axial station. This result is similar to that obtained by Holden at Mach 11 on slender blunt cones at the angle of attack [13]. Here, the bluntness effects cause the entropy layer to be swallowed more rapidly on the windward side, increasing the momentum thickness and impeding the crossflow momentum transfer and further destabilizing the wind side. These measurements were later repeated in the ground test program at both 1 and 5 deg angles of attack during the flare angle portion of the study, showing excellent run-to-run repeatability.

On the lee side of the model, the transition characteristics vary only a little between model attitudes of 0 and 1 deg and show similar transition locations. However, at a 5 deg incidence, the transition point has moved significantly forward on the cone, possibly due to a small separation bubble at the nose, resulting in turbulent heating of over 35 in. of the cone. Additional lee-side measurements were made during the flare angle studies and similarly show excellent repeatability. This repeatability has been calculated to be well within 5%. These results show that for the Mach number, Reynolds number, and angle of attack variations considered in this study the 0.098 nose bluntness is the best choice to achieve the goal of well-defined laminar, transitional, and turbulent regions during flight for code and ground test comparison and validation.

As equally important as the transition study, the first phase of the ground test was also designed to select the proper flare angle for the flight test. As with the transition part of the flight experiment, it is important to obtain flight data in a well-defined shock wave/boundary-layer interaction region so that good comparisons with ground test and computational results may be made. This requires a fully turbulent boundary layer on the cylinder surface, definable separation and reattachment regions over the cylinder flare junction,

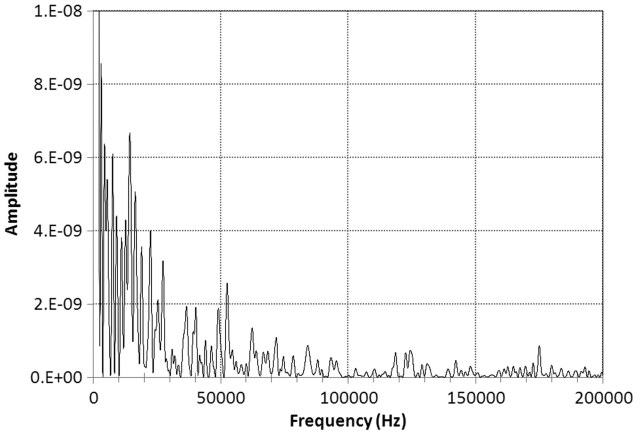

Fig. 18 Measured frequencies from flush mounted pitot pressure sensors.

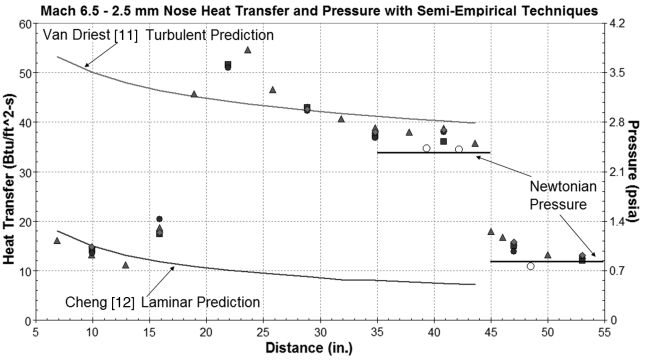

Fig. 19 Mach 6.5 and Reynolds number 5.0E6 per foot heat transfer and pressure measurements with the 0.098 in. nose configuration showing transition delayed to 15 in.

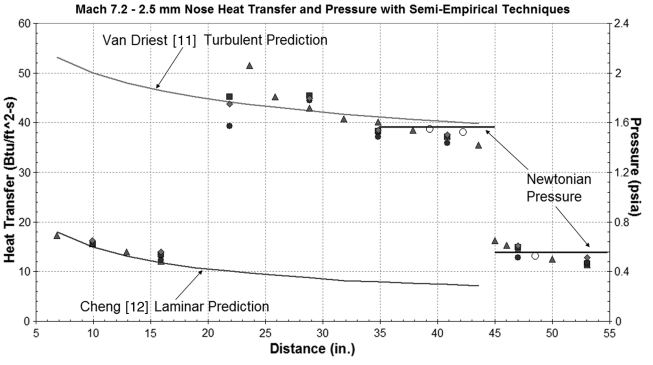

Fig. 20 Mach 7.2 and Reynolds number 3.0E6 per foot heat transfer and pressure measurements with the 0.098 in. nose configuration showing transition delayed to 18 in.

and a measurable reattached flow region over the latter part of the flare to serve as a definable boundary condition for comparison purposes. Initial pretest computations suggested a flare angle of 37 deg was appropriate for the flight vehicle, but the flow characteristics needed to be experimentally tested to confirm this choice. During this phase of the ground test, the flare was to remain uninstrumented so that changes could be quickly made while the model remained in the tunnel. Data were thus obtained employing CUBRC's high-speed schlieren video system. This system employs a copper vapor laser and a 10,000 frame per second Phantom version 7.0 camera that is synchronized to the laser pulses and is able to essentially "freeze" the flow phenomena.

Initial tests with a flight Mach number of 7.2 and Reynolds number of 3.0E6 per foot were performed with the 37 deg geometry. The schlieren images of this configuration indicated that reattachment occurred close to or at the end of the flare so that there was not a significant attached region downstream of reattachment. This would not allow measurements to be made in-flight with a definable downstream boundary condition, which is required to accurately evaluate the performance of the turbulence models employed in the predictions.

Computational and experimental [7–9] configuration studies at CUBRC before testing suggested that a 30 deg flare angle would be a good choice to obtain to the desired flow characteristics but, due to angle-of-attack concerns lengthening the separated region on the lee side of the model, it was decided to next try a flare angle at 27 deg. The schlieren images of this new angle show that the separated region is now very small and the flare shock wave extends through the boundary layer almost to the cylinder/flare junction point. This flare case would not be satisfactory for the flight case.

The 27 deg flare was then removed and replaced with a 30 deg flare angle and the model was retested at the same test conditions. The schlieren image for this condition showed a slightly larger separated region and, though this might be a good selection for angle of attack cases, it remains too small for the required flight case geometry.

The fourth and final flare angle of 33 deg was next tested at Mach 7.2. This flare angle produced a separated region, Fig. 21, that reattached about two-thirds of the way up the flare, producing a reattachment shock. These features indicate well-defined flow characteristics that can be expected to produce data downstream of the reattachment point that can be employed as a boundary condition for computationalists to validate turbulence models. Additional tests with this flare angle were then performed at the Mach 6.5 flight condition and over a range of angles of attack to further confirm that this was the proper angle to be employed on the flight vehicle.

A final part of this phase involved heating the model nose to investigate the effect of wall temperature on the transition location. Employing an electrical resistance heater installed in the removable nose tip, we heated the nose and cone section to 800°R. We also monitored the temperature gradient up the nose section using the installed thin-film sensors that, in their simplest form, are resistance thermometers. The temperature starts at 800°R at the nose and returns to room temperature by 25 in. up the nose. These temperature values were sampled immediately before tunnel operation. The resulting data compared with the unheated model data are presented in Fig. 22. Here it is shown for the conditions and temperatures tested that there is very little effect of wall temperature. The freestream values for this comparison case were both run at the Mach 7.2 flight condition.

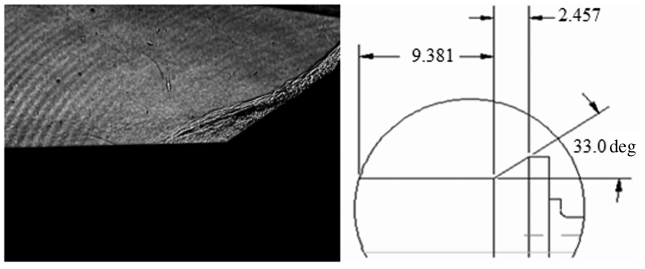

Fig. 21 Schlieren image of the flare region at Mach 7.2 and a 33 deg flare angle.

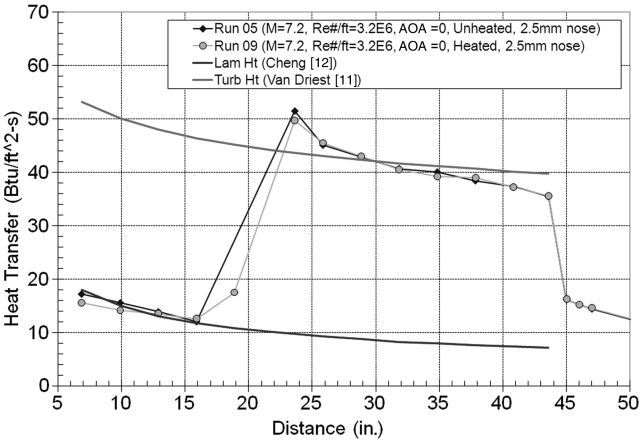

Fig. 22 Comparison of the transition location between the unheated and prerun heating of the HIFiRE-1 nose region.

VI. Experimental Results of the Current Study

A. Initial Tests and Comparison with Phase I Results

The current study began with several tests repeating the model configuration and freestream conditions to confirm matching results to the first phase of testing and to obtain high-resolution transition data at these conditions for use with the STABL stability analysis code. These initial runs were also used to check out the large amount of new instrumentation in the flare region. The cone results from the second entry are compared directly with the first entry results in Fig. 23 for the Mach 7.2 condition. The key data comparison in the figure is the open vs closed diamonds. The open diamonds represent the results from the first entry whereas the closed diamonds are the heat-flux measurements from the second entry. The most heavily instrumented ray is represented by the diamonds whereas the other shapes represent rays at 90, 180, and 270 deg around the model, showing the excellent symmetry in the transition front around the model. Agreement between the two entries is excellent in both heat-flux level and transition location. The additional heat-flux sensor locations are evident throughout the transition region and add a significant amount of resolution to the region that will be very valuable in the assessment of computational turbulence modeling.

B. Studies of Trip Effectiveness

The HIFiRE-1 flight vehicle will include a single discrete diamond-shaped roughness element located 20.7 in. (525 mm) from the blunt nose tip on the surface of the cone section. This trip has been designed to extend the region in the flight trajectory where turbulent

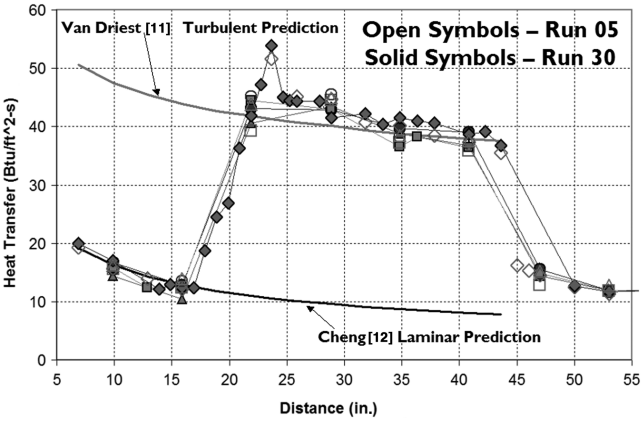

Fig. 23 Comparison of Mach 7.2 transitional heat transfer results from the first and second phases.

flow can be obtained over the surface of the model. To verify these design assumptions, a portion of the ground test program was dedicated to testing the trip effectiveness to sustain turbulent flow over the cylinder section through the expansion and assess the effects of the trip on the opposite side of the model and when the flow is naturally turbulent. The trip employed in the experimental program is shown in Fig. 24. The trip is a diamond shape with all sides equal to 0.39 in. (10 mm) in length and 0.079 in. (2 mm) in height. The corners have been rounded with a radius of 1/32 in.. The distance on the wind-tunnel model was slightly shorter than the flight location by 0.12 in. (3 mm), but this is done intentionally to place the trip directly behind a surface heat-flux sensor. The first test performed during this portion of the program consisted of a laminar smooth body baseline run. All the results from the trip effectiveness tests can be seen in Fig. 25, compared in nondimensional heat transfer coefficient form multiplied by the square root of the Reynolds number to collapse the laminar portion of the heating data. Here, the heat transfer coefficient will be defined as

$$ch = \frac{q}{\rho U(h_{\text{aw}} - h_w)}$$

where q is the measured heat flux, ρ is the freestream density, U is the freestream velocity, and h_{aw} and h_w are the adiabatic wall and wall enthalpies, respectively. The agreement in the laminar region is good and confirms the heat-flux measurements and freestream conditions.

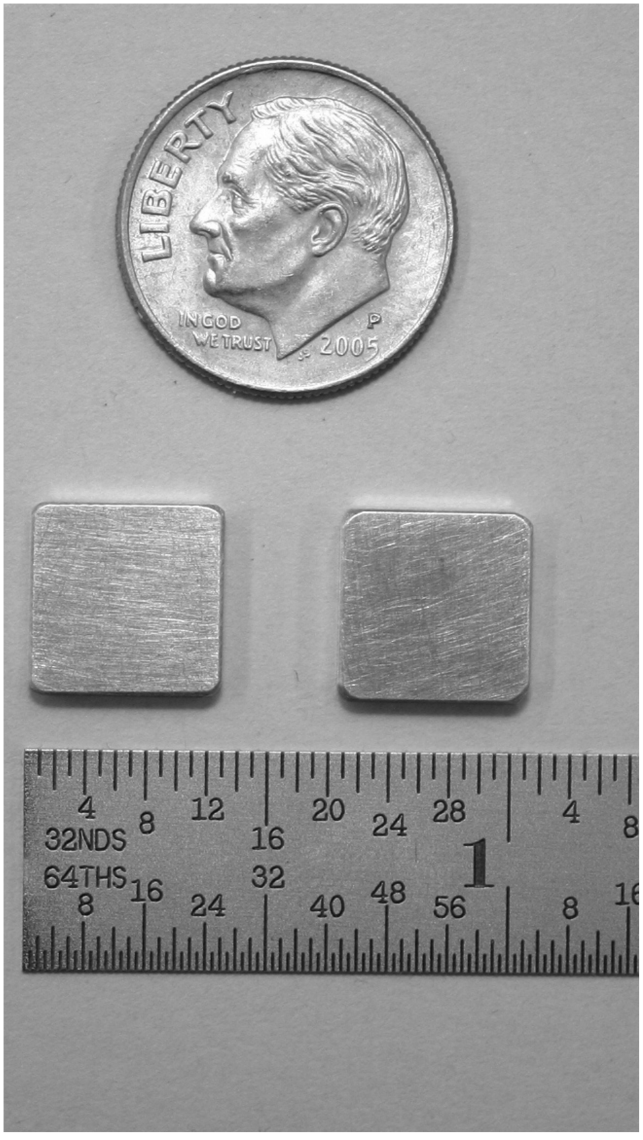

Fig. 24 Trips employed in roughness studies.

There may be some indication in the smooth wall run (solid squares) past 40 in. of the beginnings of transition, but this likely goes away as the flow expands onto the cylinder section. The trip was next applied to the surface, and tests were performed over a range of Reynolds numbers and model attitudes to assess the trip effectiveness. In Fig. 25, the trip location is evident due to the increase in heat flux directly in front of the trip element as the flow stagnates on the leading edge. At the higher Reynolds numbers, the boundary-layer transitions closer to the trip location and, conversely, as the Reynolds number is decreased, the distance between the trip and the transition location increases. At the lowest Reynolds number, the heat flux actually decreases below the laminar level due to the trip disturbance. The runs are then compared with the laminar and smooth body transition runs in a turbulent collapse form by multiplying the heat transfer coefficient by the fifth root of the Reynolds number in Fig. 26. The fifth-root Reynolds number scaling in this figure allows for the correlation and collapse of the turbulent regions of the flow. There is good collapse of all the runs on the cone section once the data at each Reynolds number complete the transition process. The collapse on the cylinder section is not as good with the solid triangles, the lowest Reynolds number condition, falling somewhere between the fully turbulent and fully laminar levels. The uncertainty in the tripped lowest Reynolds number (0.5E6 1/ft) condition on the cylinder section results in performing the rest of the tripping studies at the next higher Reynolds number (1.0E6 1/ft) to assure a well-defined test case. Figure 27 shows the discrete roughness angle-of-attack tests performed at the 1.0E6 1/ft Reynolds number condition, and effective tripping for all tested model attitudes is observed assuring turbulent flow on the cone and cylinder sections. The effect of the trip element on the opposite side of the model was also assessed at this time, but these results will be discussed later with the rest of the flare data.

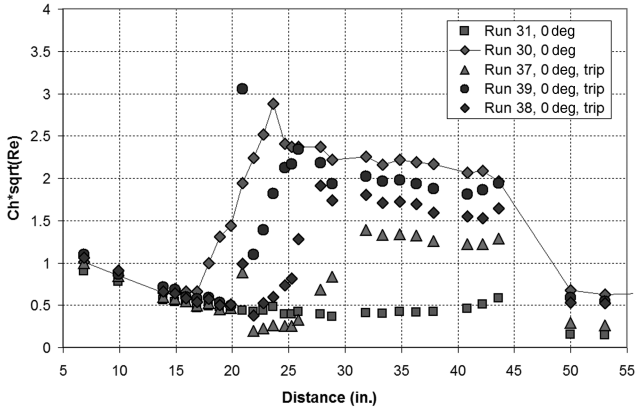

Fig. 25 Tripped run at $Re/\text{ft} = 2 \times 10^6$ compared with laminar and turbulent conditions.

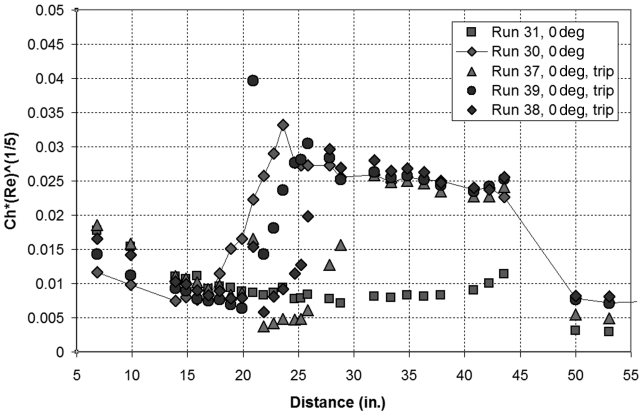

Fig. 26 Tripped runs compared with turbulent correlation.

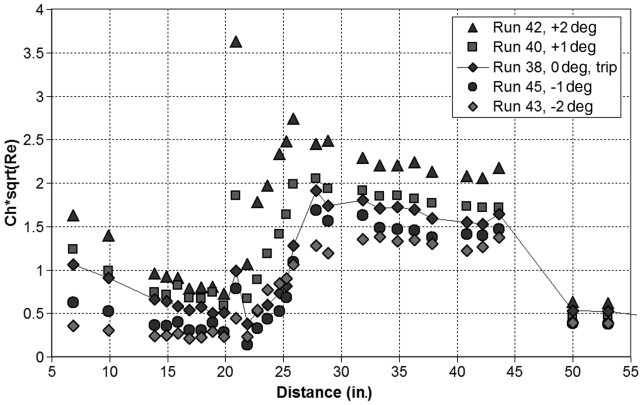

Fig. 27 Tripped angle-of-attack sweep at $Re/\mathrm{ft} = 1 \times 10^6$ freestream condition.

C. Second Entry Flare Region Heat-Flux Results

In Sec. V, the first-phase flare selection process was described in detail employing high-speed schlieren movie stills. These schlieren movie stills were also employed to lay out the instrumentation to measure the heat flux and pressure in this region during the second phase of the ground test. Two metal inserts were constructed and instrumented, with the maximum number of instruments being limited only by the physical size constraints. Pictures and drawings of these inserts can be seen in Fig. 12. Example flare data from the initial runs can be seen in Fig. 28. Here we see the initial turbulent level of heat transfer (triangle) and pressure (diamond) on the cylinder surface with a jump after 62 in. as the flow separates and then increases to a peak level at 65.5 in. during the reattachment and interaction process. Agreement between the pressure and heat transfer looks good in both the separated region and the peak interaction region. The schlieren images on the flare region between the first and second phases were also in good agreement. Though all these things were encouraging signs that the experiment was going to be a success, the lack of a well-defined boundary condition downstream of the peak region was cause for concern. The flare length in the current configuration appeared to be too short for the reattachment and compression process to complete and the flow to return to simple cone pressure levels. This boundary condition data could be the difference in the ability to properly model the turbulent flow in this region. To correct this situation, the decision was made to construct an additional flare extension that could be easily added to the already existing flare length. The data from the first run after this configuration change can be seen in Fig. 29. Here comparisons of the heat transfer and pressure from both runs are presented, and there is good agreement between the two runs in separated region length, peak location, and overall heat-flux levels; with the additional flare length, enough data should now result in a well-defined experiment that also is of code validation quality.

Upon the resolution of the flare length, the ground test program proceeded as planned. Figure 30 shows results from an angle-of-attack sweep over the anticipated flight angle-of-attack range. These studies were performed at the Mach 7.2 flight condition. The results show that at positive angles of attack, the angle of the cone and flare

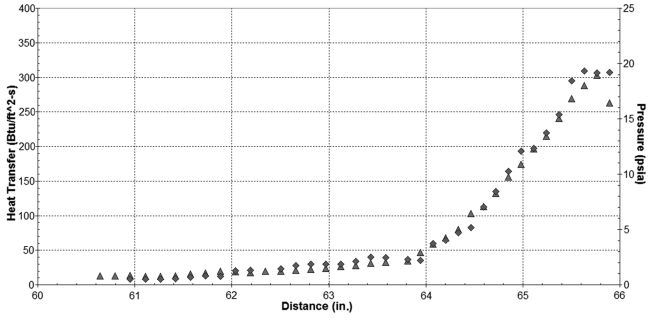

Fig. 28 Initial flare region results at freestream flight conditions.

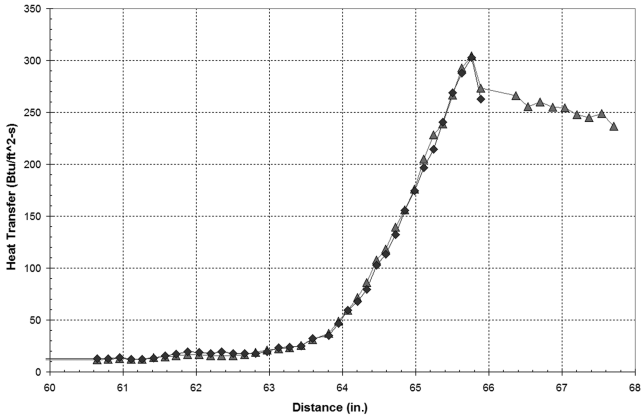

Fig. 29 Heat-flux results comparing the flight length flare and the extended length flare.

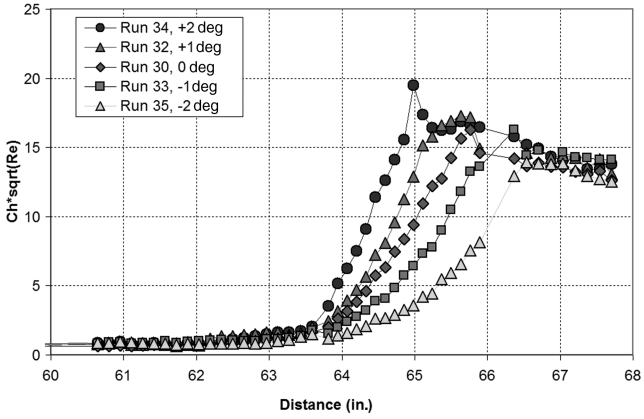

Fig. 30 Smooth body flare region heat-flux results for the flight angle-of-attack range.

sections gets larger with respect to the flow and the separated region shortens and moves the peak heating location further upstream. At negative angles of attack, the cone and flare angles get smaller with respect to the flow and, as expected, the separation regions increase in size and move the peak heating location downstream. The flight test will employ these results directly to select the appropriate flight instrumentation and determine its proper location on the flight vehicle. To satisfy this goal, several additional ground test points were selected to better define what to expect in flight and aid in the analysis of the flight data postflight. During flight, the vehicle will be spinning and have a small coning motion that results in the angle of attack. At lower Reynolds numbers, the discreet roughness element would provide transition data on one side of the model whereas the other will remain laminar. This situation needed to be verified in the ground test, and the first additional test point consisted of placing the discreet diamond roughness element on the opposite side of the test model from the detailed flare instrumentation to see if, at angle of attack, the effect of the roughness fed around the model and caused a difference in transition or the character of the interaction region on the lee side of the vehicle. This data point was again obtained with the Mach 7.2 flight condition. The results of this study, shown in Fig. 31, show no effect of the roughness on the lee side of the model.

D. Correlation of Thin-Film Transition Results with High-Speed Schlieren Movie Stills

A feature of employing thin-film heat-flux instrumentation in the transition region on the cone surface is the ability to follow the transition process from laminar to turbulent. The transition process, based on testing experience at CUBRC over the last 50 years, has been observed to be of two types. The first type can be described as "fingers" of transition that appear to move up and down stream over

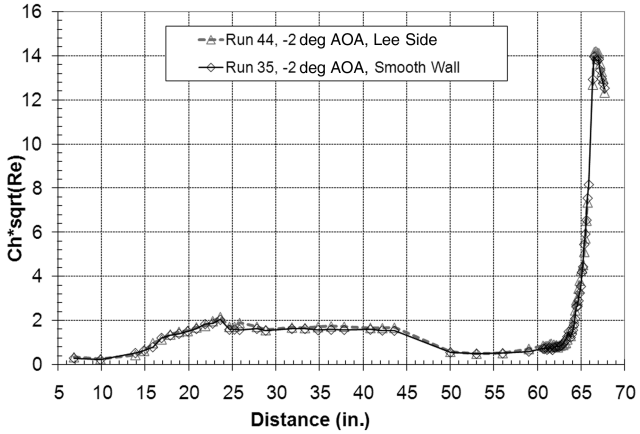

Fig. 31 Effect of lee side roughness at the angle of attack.

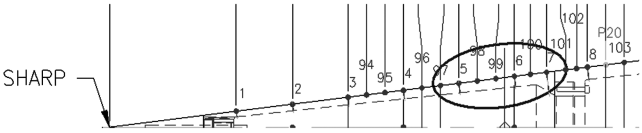

Fig. 32 Instrumentation region of interest for schlieren comparisons.

time and make up the transition front. The second type can be described as regions of turbulence bursting out and moving downstream. Other turbulent bursts break out downstream and coalesce with the upstream bursts until the entire region is fully turbulent. During the HIFiRE-1 ground test program, detailed high-speed schlieren videos were taken of the transition region on the cone and these videos have been compared with the thin-film sensors in the same region. Figure 32 shows the instrumentation layout of the HIFiRE-1 model with the circled region showing the instruments that will be compared directly to the schlieren video. Three separate snapshots in time will be presented, each showing a different part of the transition process as it occurs on HIFiRE-1 at flight conditions. The first time, Fig. 33, shown in the schlieren still (upper right), is represented in the heat-flux time history traces by a vertical line. These time history traces are compared with locations in the schlieren still with corresponding numbers. Each time history trace represents regions of laminar flow and turbulent bursts that make up the transition region. A closer look at the schlieren still shows laminar flow upstream, transition in the center, and the start of fully turbulent flow downstream. The same state can be seen in the time history traces; time history traces 1 and 2 show laminar flow whereas 3 and 4 show the heat flux approaching turbulent levels. Figure 34 catches a turbulent burst in the center of the schlieren window and, here, time history traces 2 and 3 show turbulent levels whereas 1 and 4 show levels approaching laminar. Finally, Fig. 35 shows a state in which the entire schlieren window appears to be laminar and, again, this is borne out by the time history traces each showing laminar levels at this time. These figures show the importance of having an adequate test time when analyzing the transition process.

VII. Summary of Computational Results

A. DPLR Navier–Stokes Solver

All ground test studies in the LENS facilities are extensively calibrated and validated with numerical tools. The primary CFD tool used is the DPLR code provided by the NASA Ames Research Center. DPLR is a multiblock, structured, finite volume code that solves the reacting Navier–Stokes equations, including finite rate chemistry and finite rate vibrational nonequilibrium effects. This code is based on the data-parallel line relaxation method [14] and implements a modified (low dissipation) Steger–Warming flux splitting approach [15] for the convection terms and central differencing for the diffusion terms. The finite rate vibrational relaxation is modeled via a simple harmonic oscillator vibrational degree of freedom [16] using the Landau–Teller model [17]. The vibrational energy relaxation rates are computed by default from the semi-empirical expression of Millikan and White [18], but rates from

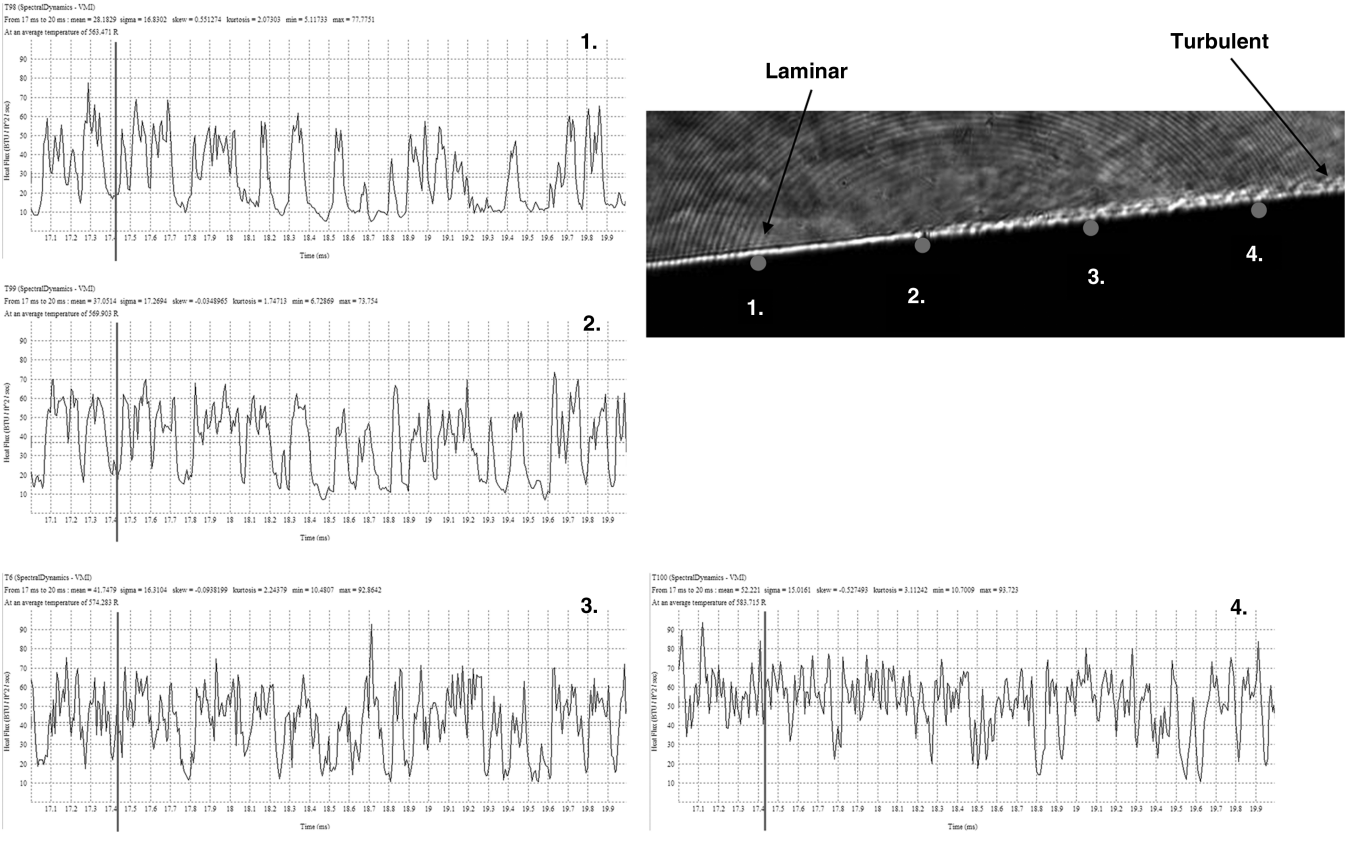

Fig. 33 Schlieren video still frame with corresponding time history trance showing transition from laminar to turbulent flow.

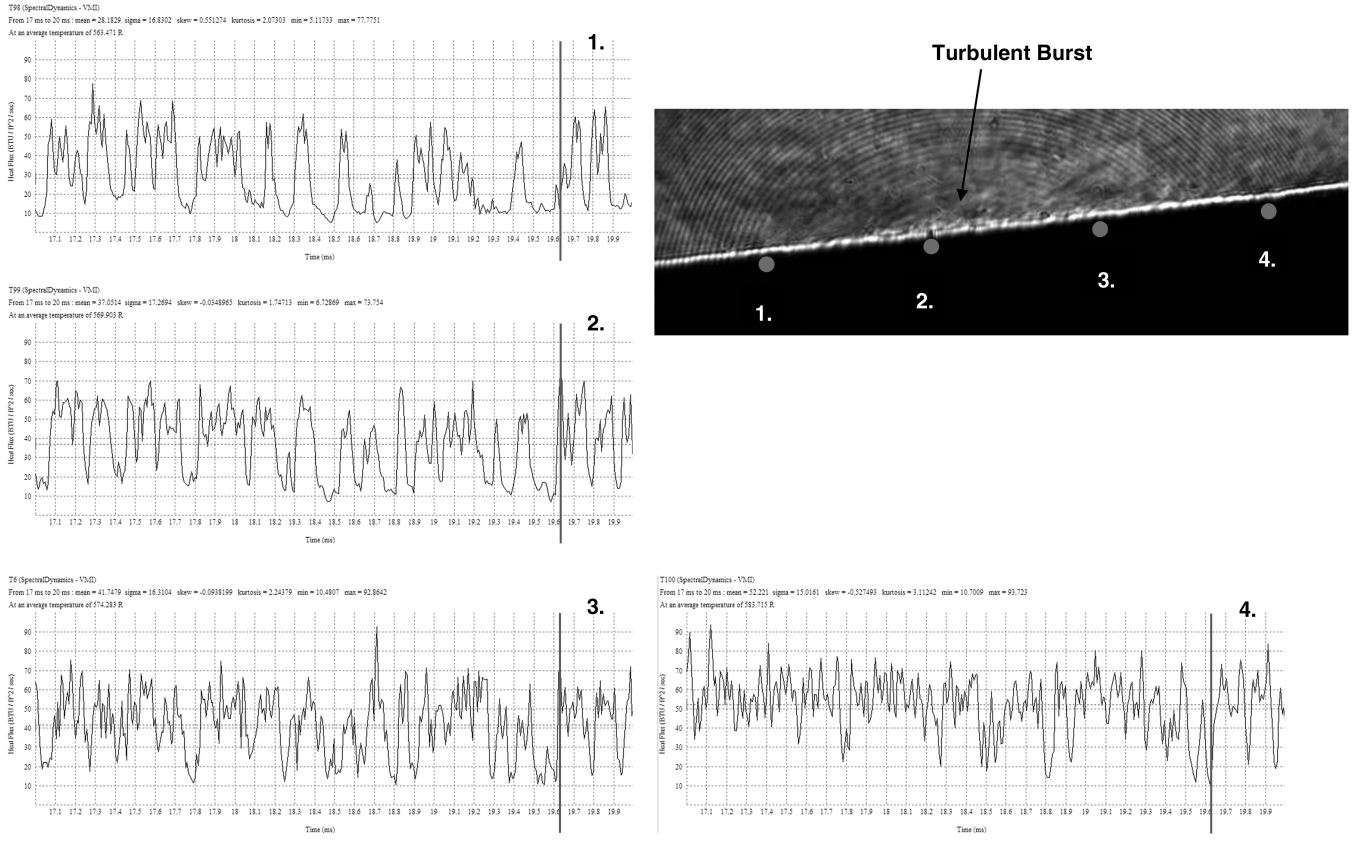

Fig. 34 Schlieren video still frame with corresponding time history trance showing a turbulent burst in the center of the window.

the work of Camac [19] and Park et al. [20] are substituted for specific collisions where experimental data exist. Vibration-dissociation coupling is currently modeled using the T–Tv approach of Park [21] or with some preliminary implementation of vibration–dissociation–vibration coupling [22]. Transport properties are appropriately modeled in DPLR for high-enthalpy flow [23,24] using the binary collision-integral-based mixing rules from Gupta et al. [25]. Diffusion coefficients are modeled using the self-consistent effective

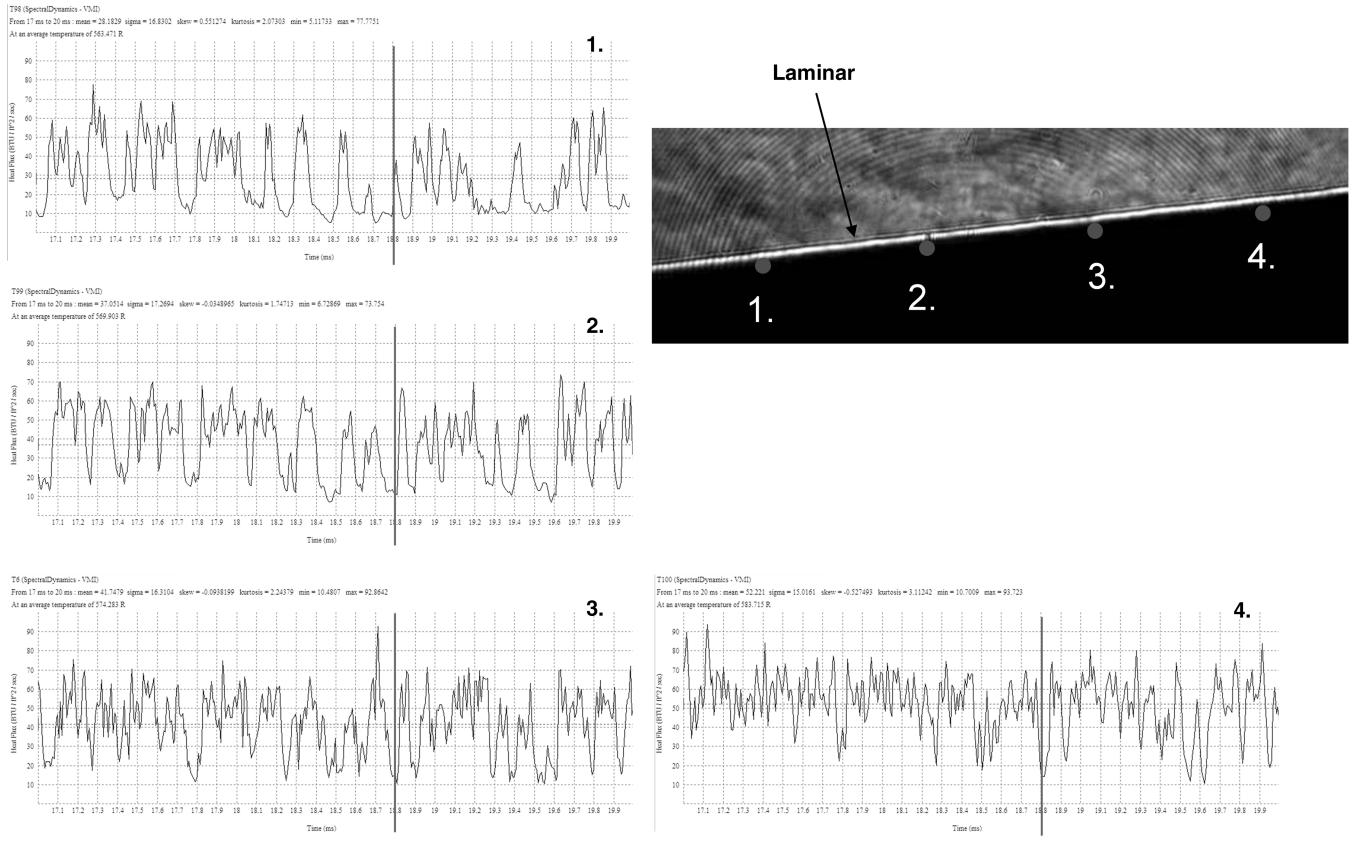

Fig. 35 Schlieren video still frame with corresponding time history trance showing laminar flow across the window.

binary diffusion method [26]. Turbulence models available in the DPLR code currently include the Baldwin–Lomax zero-equation model [27], the Spalart–Allmaras single-equation model [28], and the shear stress transport two-equation model [29], each with corrections for compressibility effects [30,31]. Additional DPLR code capabilities with relevance to this study involve automated grid adaptation to improve solution quality [32].

B. STABL Tool Package/PSE–Chem Solver

The STABL package [33–35] is a comprehensive suite of tools that features an integrated two-dimensional/axisymmetric chemically reacting laminar flow solver, an equilibrium chemistry solver, a parabolized stability solver, a postprocessor, and various supporting tools and scripting wizards integrated into a single, intuitive, Perl-based graphical user interface. The CFD and parabolized stability equation (PSE) solvers use message passing interface for efficient parallel processing. STABL was developed at the University of Minnesota (a combination of versions 2.4 and 2.6 were used for these analyses).

The PSE–Chem solver is a primary part of the STABL suite that solves the parabolized stability equations for two-dimensional or axisymmetric flow derived from the Navier–Stokes equations. The PSE equations are developed by modeling instantaneous flow variables with a mean and fluctuating component and subtracting the mean component from the resulting equation set. The result is a system of second-order partial differential equations for the disturbances, which are parabolized according to the method of Herbert [36] by assuming that the disturbances are composed of a fast-oscillatory wave part and a slowly varying shape function. The ellipticity of the wave part is preserved whereas only the governing equation for the shape function is parabolized. Assuming that the initial disturbances are small and making an assumption of a "locally parallel" flow at the starting plane allows sufficient simplification to generate an initial solution for the shape function and complex streamwise wave number. These initial solutions may then be marched downstream by integrating the parabolized stability equations.

The PSE analysis generates a prediction for the evolution of an initial disturbance as it moves downstream from its starting point through the mean flowfield. To predict the onset of transition, an experimental correlation is required. PSE–Chem uses the semi-empirical e^N correlation method.

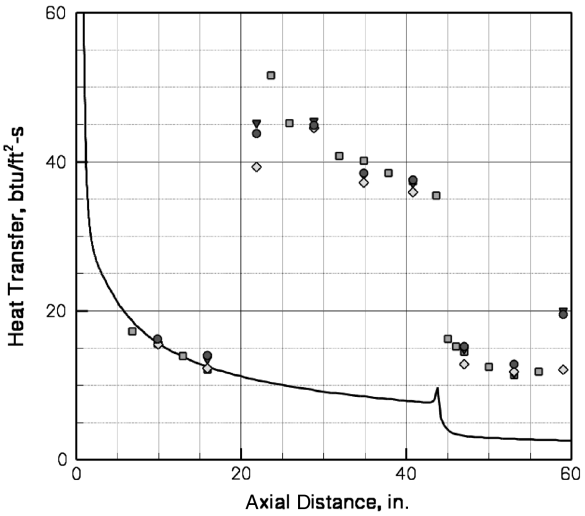

Fig. 36 Mach 7.2 laminar DPLR solution of the 0.098 in. nose case.

C. Comparisons of Laminar DPLR Solutions with Experimental Data

In parallel with the experimental testing, CUBRC also performed a computational analysis of the pressure and heating levels on both the cone and cylinder areas of the model. The laminar solutions were compared directly with the baseline laminar levels in the experiment before transition and were used to help guide the experimental program and add confirmation to the experimental freestream conditions and model data. These laminar solutions would later be imported directly into the STABL code and used in the stability calculations. Examples of laminar comparisons for both test conditions with the 0.098 in. (2.5 mm) nose bluntness can be seen in Fig. 36. These comparisons show excellent agreement in the laminar flow region ahead of transition. This figure also shows the excellent agreement between the four rays of the model. The rise in the data near the 60 in. portion of the plot is due to the flare-induced separated region and changes from run to run as the flare angle is being modified.

D. Employing the DPLR and STABL Codes to Estimate Transition Behavior on Flight Vehicle

The extrapolation of the ground test measurements to the flight conditions using the STABL code provided an extremely valuable approach to employing ground test measurements to support the design of flight vehicles. In essence, the measurements made in the ground test environment are employed to calibrate the STABL code, which is then employed to determine the magnitude of the perturbation to transition position for N factors, which have been suggested from flight data. The DPLR code is first employed to

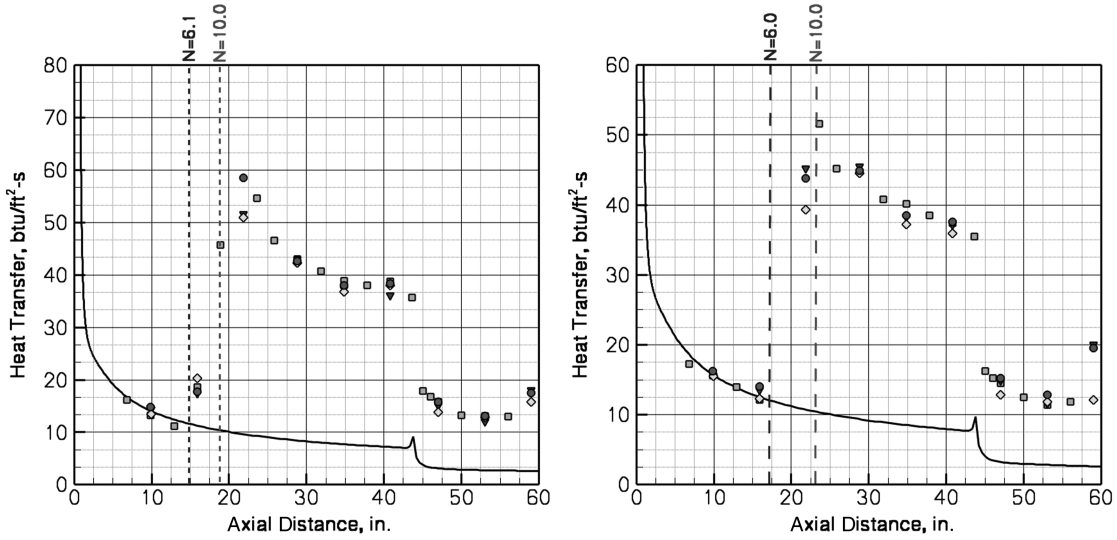

Fig. 37 Predictions of the downstream movement of transition from ground test to flight: a) Mach 6.5 (run 4), and b) Mach 7.2 (run 5).

predict the flow over the blunt cone configuration. The STABL code then solves the PSE for the growth of the first- and second-mode instabilities by the integration of the disturbance using an e^N fit. Previous studies have indicated that typical values for N are 5.5 in the wind tunnel, and current thinking puts the value between 8 and 11 for flight vehicles, but there is a large amount of uncertainty in this flight range. A stability map is created, which then is employed to plot an N-factor axial distance envelope. An N factor for the ground test measurements is calculated based upon the measurements of incipient transition and, by employing flight N factors of typically 10, one can extrapolate to determine the delay in transition expected for the flight case. Two examples of the extrapolation to flight using this approach are shown in Figs. 37a and 37b for the flight Mach number 6.5 and 7.2 test conditions, respectively. These calculations have been performed by MacLean at CUBRC using the aforementioned method and have been reported in [1]. For the Mach 6.5 condition shown in Fig. 37a, this extrapolation technique indicates that transition would move downstream on the cone by approximately 4.5 in. from its measured location at 15 in. Clearly, this is a small increment on the 45 in. cone and would support our conclusion that the model configuration proposed for the flight test was completely acceptable. A similar set of calculations at the 7.2 condition are shown in Fig. 37b and, again, the predicted 4 in. movement of the transition point would not significantly influence our selection of the flight configuration. A second calculation by Johnson et al. [37], employing a similar approach, yielded results that compared very well to the results by MacLean described herein. To reiterate, this is an important result because it gives confidence that the appropriate nose shape has been chosen for the flight case to give the desired laminar and turbulent regions on the cone section of the flight vehicle.

VIII. Conclusions

Experimental studies have been conducted in hypersonic flows to provide measurements with which to evaluate and improve the modeling of turbulence phenomena associated with boundary-layer transition and shock wave/boundary-layer interaction. These studies were conducted at fully duplicated flight conditions in the LENS I tunnel, employing full-scale models of the flight vehicle and components. The studies conducted for the AFRL- and AFOSR-sponsored HIFiRE-1 program were designed to aid in the selection of the configuration to be employed in the flight-test program. Schlieren photographs and detailed heat transfer measurements were made to determine the characteristics of regions of boundary-layer transition and shock wave/boundary-layer interaction over the conical forebody and cylinder/flare section of the model. These measurements, together with the numerical computations using the DPLR code, were employed to select a 0.098 in. (2.5 mm) nose-tip radius and a 33 deg flare angle for the flight vehicle, as well as verify that the overall length and geometry of the conical, cylindrical, and flare sections of the model would provide valuable data for the flight-test program. Flight vehicle geometry selections were further reinforced by stability calculations obtained employing the STABL code, which predicted only several inches of downstream movement of the transition point in flight compared with the ground test.

Acknowledgments

This work was supported by the U.S. Air Force Office of Scientific Research under grant FA9550-04-1-0341, subcontract M5146247101. The authors would like to acknowledge the support and guidance of Peter Erbland, Roger Kimmel, and David Adamczak of the U.S. Air Force Research Laboratories in Dayton, Ohio, and John Schmisseur of the U.S. Air Force Office of Scientific Research. Experimental work and analysis performed during this program was supported and directed under contract to the AFOSR and AFRL.

References

[1] MacLean, M., Wadhams, T., and Holden, M., "A Computational Analysis of Ground Test Studies of the HIFiRE-1 Transition Experiment," *46TH Aerospace Sciences Meeting & Exhibit. Reno, NV*, AIAA Paper 2008-0641, 7–10 January 2008.

[2] AAEC Research Staff, "LENS Brochure," Capabilities and Technologies, Buffalo, NY, 2004.

[3] Vidal, R. J., "Model Instrumentation Techniques for Heat Transfer and Force Measurements in a Hypersonic Shock Tunnel," Cornell Aeronautical Laboratory, Report AD-917-A-1, Feb. 1956.

[4] Cook, W. J., and Felderman, E. J., "Reduction of Data from Thin-Film Heat-Transfer Gages: A Concise Numerical Technique," *AIAA Journal*, March 1966, pp. 561–562.

[5] Estorf, M., Radespiel, R., Schneider, S., Johnson, H., and Hein, S., "Surface-Pressure Measurements of Second-Mode Instability in Quiet Hypersonic Flow," *46TH Aerospace Sciences Meeting & Exhibit. Reno, NV*, AIAA Paper 2008-0641, 7–10 January 2008.

[6] Kimmel, R., Adamczak, D., Gaitonde, D., Rougeux, A., and Hayes, J., "HIFiRE-1 Boundary Layer transition Experiment Design," *45TH Aerospace Sciences Meeting & Exhibit. Reno, NV*, AIAA Paper 2007-0534, January 2007.

[7] Holden, M. S., "Shock-Wave Turbulent Boundary Layer Interaction in Hypersonic Flow," *Paper presented at the AIAA 10th Aerospace Sciences Meeting, San Diego, CA*, AIAA Paper 72-74, 17–19 January 1972.

[8] Holden, M. S., and Moselle, J. R., "Theoretical and Experimental Studies of the Shock Wave-Boundary Layer Interaction on Compression Surfaces in Hypersonic Flow," Calspan, Report No. AF-2410-A-1, October 1969; also ARL Paper 70-0002, January 1970.

[9] Holden, M. S., "A Review of Aerothermal Problems Associated with Hypersonic Flight," *Paper presented at the AIAA 24th Aerospace Sciences Meeting, Reno, Nevada*, AIAA Paper 86-0267, 6–9 January 1986.

[10] Wadhams, T., MacLean, M., Holden, M., and Mundy, E., "Pre-flight Ground testing of the Full-scale FRESH FX-1 at Fully Duplicated Flight Conditions," *37TH AIAA Fluid Dynamics Conference & Exhibit. Miami, FL*, AIAA Paper 2007-4488, 25–28 June 2007.

[11] Van Driest, E. R., "Turbulent Boundary Layer in Compressible Fluids," *Journal of the Aeronautical Sciences*, Vol. 18, March 1951, pp. 145–160.

[12] Cheng, H. K., Hall, G., Gollian, T. C., and Hertzberg, A., "Boundary-Layer Displacement and Leading-Edge Bluntness Effects in High-Temperature Hypersonic Flow," *Journal of the Aero/Space Sciences*, Vol. 28, May 1961, pp. 353–381.

[13] Holden, M. S., "Measurements of Boundary Layer Transition on Cones at Angle of Attack for Mach Numbers from 11 to 13," *26th AIAA Fluid Dynamics Conference in San Diego, CA*, AIAA Paper 1995-2294, 19–22 June, 1995.

[14] Wright, M. J., Bose, D., and Candler, G. V., "A Data Parallel Line Relaxation Method for the Navier-Stokes Equations," *AIAA Journal*, Vol. 36, No. 9, Sept 1998, pp. 1603–1609. doi:10.2514/2.586

[15] MacCormack, R. W., and Candler, G. V., "The Solution of the Navier-Stokes Equations Using Gauss-Seidel Line Relaxation," *Computers and Fluids*, Vol. 17, No. 1, 1989, pp. 135–150. doi:10.1016/0045-7930(89)90012-1

[16] Candler, G. V., "Chemistry of External Flows," *Aerothermochemistry for Hypersonic Technology*, Von Karman Institute for Fluid Dynamics Lecture Series, VKI LS, Brussels, 1995-04.

[17] Landau, L., and Teller, E., "Theory of Sound Dispersion," *Physikalische Zeitschrift der Sowjetunion*, Vol. 10, No. 34, 1936.

[18] Millikan, R., and White, D., "Systematics of Vibrational Relaxation," *Journal of Chemical Physics*, Vol. 39, No. 12, 1963, pp. 3209–3213. doi:10.1063/1.1734182

[19] Camac, M., "CO_2 Relaxation Processes in Shock Waves," *Fundamental Phenomena in Hypersonic Flow*, edited by J.G. Hall, Cornell Univ. Press, Ithaca, NY, 1964, pp. 195–215.

[20] Park, C., Howe, J. T., Jaffe, R. J., and Candler, G. V., "Review of Chemical-Kinetic Problems of Future NASA Missions II: Mars Entries," *Journal of Thermophysics and Heat Transfer*, Vol. 8, No. 1, 1994, pp. 9–23. doi:10.2514/3.496

[21] Park, C., "Assessment of Two-temperature Kinetic Model for Ionizing Air," *AIAA 22ND Thermophysics Conference. Honolulu, HI*, AIAA Paper 87-1574, 8–10 June 1987.

[22] Marrone, P. V., and Treanor, C. E., "Chemical Relaxation with Preferential Dissociation from Excited Vibrational Levels," *The Physics of Fluids*, Vol. 6, No. 9, September 1963, pp. 1215–1221. doi:10.1063/1.1706888

[23] Palmer, G. E., and Wright, M. J., "A Comparison of Methods to Compute High Temperature Gas Viscosity," *Journal of Thermophysics*

and Heat Transfer, Vol. 17, No. 2, 2003, pp. 232–239.
doi:10.2514/2.6756

[24] Palmer, G. E., and Wright, M. J., "A Comparison of Methods to Compute High Temperature Gas Thermal Conductivity," AIAA Paper 2003-3913, Jun 2003.

[25] Gupta, R., Yos, J., Thompson, R., and Lee, K., "A Review of Reaction Rates and Thermodynamic and Transport Properties for an 11-Species Air Model for Chemical and Thermal Nonequilibrium Calculations to 30000 K," NASA RP-1232, August 1990.

[26] Ramshaw, J. D., "Self-consistent Effective Binary Diffusion in Multicomponent Gas Mixtures," *Journal of Non-Equilibrium Thermodynamics*, Vol. 15, No. 3, 1990, pp. 295–300.

[27] Baldwin, B. S., and Lomax, H., "Thin Layer Approximation and Algebraic Model for Separated Turbulent Flows," Huntsville, AL, AIAA Paper 78-0257, 1978.

[28] Spalart, P. R., and Allmaras, S. R., "A One-Equation Turbulence Model for Aerodynamic Flows," *30TH Aerospace Sciences Meeting & Exhibit. Reno, NV*, AIAA Paper 92-0439, 6–9 Jan, 1992.

[29] Menter, F. R., "Two-Equation Eddy-Viscosity Turbulence Models for Engineering Applications," *AIAA Journal*, Vol. 32, No. 8, August 1994, pp. 1598–1605.
doi:10.2514/3.12149

[30] Brown, J., "Turbulence Model Validation for Hypersonic Flow," *8TH Thermophysics and Heat Transfer Conference. St. Paul, MN*, AIAA Paper 2002-3308, 24–26 Jun 2002.

[31] Catris, S., and Aupoix, B., "Improved Turbulence Models for Compressible Boundary Layers," *2ND Theoretical Fluid Mechanics Meeting: Albuquerque, NM*, AIAA Paper 98-2696, June 1998.

[32] Saunders, D., Yoon, S., and Wright, M., "An Approach to Shock Envelope Grid Tailoring and Its Effect on Reentry Vehicle Solutions," *45TH Aerospace Sciences Meeting & Exhibit. Reno, NV*, AIAA Paper 2007-0207, 8–11 January 2007.

[33] Johnson, H. B., "Thermochemical Interactions in Hypersonic Boundary Layer Stability," Ph.D. Thesis, University of Minnesota, Minneapolis, MN, 2000.

[34] Johnson, H., and Candler, G., "Hypersonic Boundary Layer Stability Analysis Using PSE-Chem," *35TH AIAA Fluid Dynamics Conference and Exhibit, Toronto, ON*, AIAA Paper 2005-5023, June 2005.

[35] Johnson, H., and Candler, G., "Analysis of Laminar-Turbulent Transition in Hypersonic Flight Using PSE-Chem," *36TH AIAA Fluid Dynamics Conference and Exhibit, San Francisco, CA*, AIAA Paper 2006-3057, 5–8 June 2006.

[36] Herbert, T., "Boundary Layer Transition—Analysis and Prediction Revisited," AIAA Paper 91-0737, January, 1991.

[37] Johnson, H., Alba, C., Candler, G., MacLean, M., Wadhams, T., and Holden, M., "Boundary Layer Stability Analysis to Support the HiFiRE Transition Experiment," *45TH Aerospace Sciences Meeting & Exhibit. Reno, NV*, AIAA Paper 2007-0311, 8–11 January 20.

R. Kimmel
Associate Editor